

Ultrafast demagnetization and precession in permalloy films with varying thicknessSurya Narayan Panda,^{*} Sucheta Mondal[✉],^{*} Sudip Majumder, and Anjan Barman[†]*Department of Condensed Matter and Materials Physics, S. N. Bose National Centre for Basic Sciences,
Block JD, Sector-III, Salt Lake, Kolkata 700106, India* (Received 15 June 2023; revised 22 August 2023; accepted 5 October 2023; published 18 October 2023)

Excitation by a femtosecond laser pulse is an efficient method to control various ultrafast spin manipulation processes, e.g., ultrafast demagnetization, remagnetization, and damping. Thus, a comprehensive study of magnetization dynamics over a broad timescale by varying the excitation energy can provide a solid foundation of integrating these processes within a single system. Here, time-resolved magneto-optical Kerr effect magnetometry is used to investigate the evolution of magnetization dynamics from femtosecond- to nanosecond timescale in Ni₈₀Fe₂₀ thin films. The correlation between ultrafast demagnetization time and fast remagnetization time with the laser pump fluence is demonstrated experimentally and is validated by the phenomenological three-temperature modeling involving different coupling parameters and specific heat of electron-, lattice-, and spin baths. Significant enhancement of the Gilbert damping parameter and a redshift in the precessional frequency are observed for uniform Kittel mode and perpendicular standing spin-wave modes with increasing excitation energy. Direct correlation between demagnetization time and Gilbert damping parameter indicates spin-flip scattering as the responsible mechanism for the ultrafast demagnetization and intraband conductivity-like contribution to the damping process. This extensive study develops an in-depth understanding about the role of laser fluence on the ultrafast spin dynamics. Our findings will be beneficial for the construction of ultrahigh-speed spintronics devices which rely on the heat-assisted modification of the dynamic properties in ferromagnetic thin films.

DOI: [10.1103/PhysRevB.108.144421](https://doi.org/10.1103/PhysRevB.108.144421)**I. INTRODUCTION**

The demand for developing energy-efficient, cost-effective, and high-speed magnetic memory and storage devices has reinforced an upsurge in the fundamental research related to ultrafast magnetization dynamics in magnetic thin films, heterostructures, and nanostructures [1,2]. Continuous development in this field makes the clock speed of the processors enter the sub-GH range while increasing the storage capacity in the spin-based devices [3,4]. However, this development hits a bottleneck due to the constraints imposed by the relaxation processes involved in the magnetization dynamics which eventually limit the data-transfer rate in the device. Precessional magnetization dynamics of the ferromagnetic materials follow the Landau-Lifshitz-Gilbert equation where the rate of energy dissipation from spin-wave modes to the adjacent thermal baths can be expressed by the Gilbert damping parameter (α), which is analogous to the Rayleigh energy dissipation function [5,6]. Both intrinsic and extrinsic mechanisms contribute to the damping [7]. The spin-flip scattering (SFS) from phonons in ferromagnetic system is an example of the intrinsic scattering which cannot be reduced to zero [8]. Extrinsic contribution to α originates from additional magnon-phonon and magnon-magnon scatterings introduced to the system by doping, capping, perturbation from spin current, eddy current loss, and external temperature [9–13]. Controlling damping is of utmost

importance as a low- α value helps to reduce the write current in important applications like spin transfer torque-based magnetoresistive random access memory. On the other hand, a high- α value is necessary to eliminate the “ringing” effect after switching the magnetic states.

On a shorter timescale, ultrafast demagnetization is one of the fastest spin manipulation mechanisms which can revolutionize the field of spintronics by decreasing the switching time of the magnetization by many orders [14]. However, the true microscopic mechanisms responsible for this ultrafast loss of magnetization remain highly debatable to date. Substantial experimental and theoretical research over the last two decades have unraveled the existence of two predominant mechanisms. The first one involves the SFS process, such as Elliott-Yafet-like electron-phonon scattering [15], relativistic spin-flip scattering [16], Coulomb scattering [17] and electron-magnon scattering [18], etc., due to the direct light-matter interaction. The other presiding contribution comes from the laser-excited hot electrons through the transportation of spin current [19]. Although the timescales of ultrafast demagnetization and precessional dynamics differ by orders of magnitude, recent developments in this direction have established a correlation between these two fundamental phenomena [20]. The correlation between the ultrafast demagnetization time (τ_m) and α provides insights for identifying the dominant microscopic contribution to the ultrafast demagnetization [21,22]. A proportional relation manifests dominant local SFS contribution, while an inverse dependence signifies the contribution from the spin transport in the system. Interestingly, this correlation also helps to determine the major microscopic contribution to the damping [23]. A linear

^{*}These authors contributed equally to this work.[†]abarman@bose.res.in

relationship between τ_m and α points to the dominance of intraband conductivity-like contribution, whereas an inverse relationship indicates the interband resistivity-like contribution. It is important to mention here that the excitation with an optical pump not only leads to the generation of uniform precessional mode but also perpendicular standing spin-wave (PSSW) modes in a relatively thick magnetic layer. These modes are highly exchange dominated and reside across the thickness of the film. For this reason, PSSWs are used primarily to study the exchange interactions [24], determining the exchange stiffness constant [25], depth-dependent saturation magnetization profile, and damping [26]. Recently, PSSWs have been used in reducing the switching field of a highly coercive magnet [27]. Thus, controlling the dynamic properties of these high-frequency SW modes is extremely important.

In this paper, we have investigated the effects of pump fluence (F) on the τ_m , fast remagnetization time (τ_e) and α for, respectively, 50- and 100-nm-thick Ni₈₀Fe₂₀ (permalloy: Py hereafter) films using the time-resolved magneto-optical Kerr effect (TR-MOKE) magnetometry [28]. TR-MOKE offers several advantages over alternative techniques. It is the only technique which can provide a broad range of temporal dynamics like ultrafast demagnetization, relaxation, precession, and damping from a single measurement [29]. Besides, it is devoid of delicate microfabrication and broad area averaging. It eliminates inhomogeneous line broadening and prevents the overestimation of α . On the other hand, being a low coercive field magnet with negligible magnetostriction and magnetic anisotropy, Py is a preferred material for magnetic recording head sensors, high-frequency transformers, and several other device applications [30]. Moreover, this study provides the ultrafast spin dynamics in relatively thicker films in the presence of additional dissipation mechanisms and multiple spin-wave modes. The experimental results of the ultrafast demagnetization have revealed a monotonic increase of τ_m and τ_e with pump fluence. From the picosecond precessional dynamics, we have observed that α for both Kittel and PSSW modes remain invariant with the external magnetic field strength, but it exhibits strong enhancement with pump fluence. Instantaneous increase of the system temperature and the subsequent dissipation of heat from the probed area result in a temporal chirping of the oscillatory Kerr signal. As a result, the precessional frequencies for both the Kittel and the PSSW modes experience redshift. A direct correlation between τ_m and α indicates that SFS can be the dominant microscopic mechanism for ultrafast demagnetization and a major intraband conductivity-like contribution to α . These findings will trigger further research interest about the energy requirements and timescales of the magnetic processes in the technologically important magnetic materials.

II. SAMPLE PREPARATION AND CHARACTERIZATIONS

A. Sample preparation

Py films having thicknesses of 50 and 100 nm were deposited using a DC magnetron sputtering system (base pressure $\approx 3 \times 10^{-7}$ Torr, argon pressure ≈ 0.5 mTorr, and deposition rate ≈ 0.2 Å/s) over 8×8 -mm² silicon (100) wafers having 285-nm-thick SiO₂ coatings. Thereafter, SiO₂ capping

layers of 5 nm were deposited on top of the Py layer using rf magnetron sputtering. Very slow deposition rates were maintained to achieve uniform thicknesses of the films. Py was deposited at a DC voltage of 430 V, while SiO₂ capping layer was deposited at an average rf power of 60 W. All the other deposition conditions were carefully optimized and kept almost identical for both samples.

B. Characterization

The static magnetic properties, such as coercive field (H_c), saturation field (H_s), and saturation magnetization (M_s) of the two films were characterized using vibrating sample magnetometry (VSM). The grazing-incidence x-ray-diffraction (GI-XRD) technique was used to obtain the crystal structure. The thickness, surface roughness, and electron density of different layers were determined by x-ray reflectivity (XRR) measurement. The surface topography of the films was measured using atomic force microscopy (AFM). TR-MOKE magnetometry was used to study the magnetization dynamics from femtosecond to nanosecond timescale. The second harmonic (wavelength = 400 nm, repetition rate = 1 kHz, pulse width > 35 fs) of an amplified femtosecond laser pulse generated from a regenerative amplifier system was used to excite the dynamics, while the fundamental laser beam (wavelength = 800 nm, repetition rate = 1 kHz, pulse width ≈ 35 fs) was utilized to probe the time-dependent Kerr rotation in the polar geometry. Pump and probe beams have spot sizes of about 350 and 100 μm , respectively. Before laser pulse excitation, a strong bias magnetic field (H) was applied at a small angle ($\sim 15^\circ$) to the sample plane which ensures a finite demagnetizing field component along the pump-pulse direction. It helps to induce precessional dynamics in the sample upon optical excitation. This out-of-plane (OOP) component plays an important role in determining the initial canting angle of the magnetization which eventually influences the precessional angle. If the OOP component of magnetic field is set to zero, no optically triggered precession will be observed [31]. The back-reflected probe beam was fed to a set of an analyzer and a photodiode. The polar Kerr signal was finally detected using a lock-in amplifier in a phase-sensitive manner. Throughout the measurement, probe fluence was kept fixed at 1 mJ/cm² while pump fluence was varied over a broad range from 4 to 20 mJ/cm². All the measurements were performed at room temperature under ambient conditions.

III. RESULTS AND DISCUSSION

A. Static characterization

We have measured the in-plane (INP) and OOP magnetic hysteresis loops using VSM at room temperature for Sub/Py (50, 100)/SiO₂(5) as shown in Fig. 1(a). Thickness values indicated in the parentheses are in nanometers. The values of H_s in INP and OOP configurations for these films are about 50.0 Oe and 10.6 kOe, which reveal that these films are IP magnetized with no OOP anisotropy. We have obtained the value of M_s to be about 800 emu/cc for both the films. Also, these films exhibited small H_c (~ 15 Oe), which reveal their soft-ferromagnetic nature.

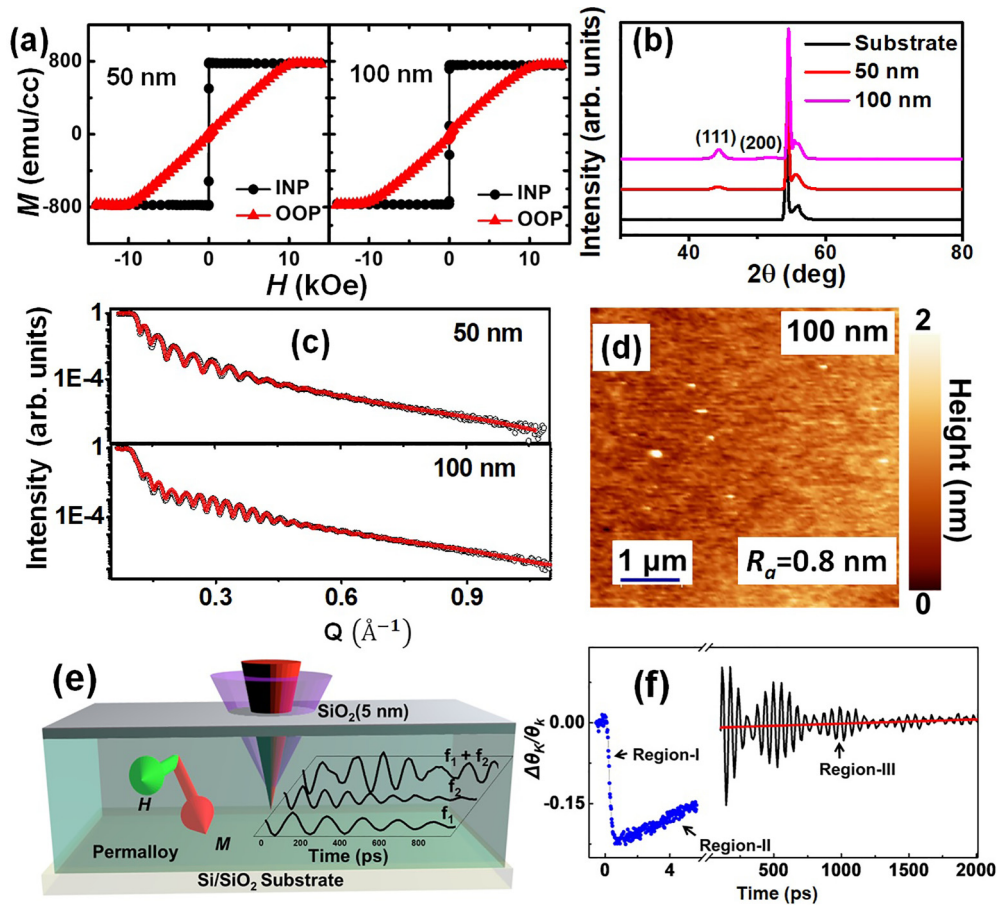


FIG. 1. (a) VSM loops for Sub/Py (50, 100 nm)/SiO₂ (5 nm) samples. (b) XRD spectra measured at 2° grazing incidence angle from bare Si/SiO₂ substrate and Sub/Py (50, 100 nm)/SiO₂ (5 nm) samples. (c) XRR spectra (symbols) for Sub/Py (50, 100 nm)/SiO₂ (5 nm) samples fitted using GENX (solid red lines). (d) Two-dimensional AFM image for Sub/Py(100)/SiO₂(5) sample. (e) Schematic of sample structure and experimental geometry. (f) Representative TR-MOKE data for Sub/Py (50 nm)/SiO₂(5 nm) sample at an applied magnetic field of 2.4 kOe and pump fluence of 10 mJ/cm² with three different temporal regimes marked in figure. Solid red line indicates exponential background.

Figure 1(b) displays the GI-XRD spectra obtained from bare Si/SiO₂ substrate and Sub/Py (50, 100)/SiO₂(5) thin films at a glancing angle of 2°. In this plot, the peaks corresponding to the 2θ angle of ~44.43° and ~51.61° primarily correspond to the (111) and (200) orientation of Py signifying the polycrystalline nature of our films [32–34]. The other high-intense peaks correspond to 2θ angles of ~54.57° and ~55.53° appear from the substrate. From the (111) peak, we have also estimated the grain size, using Scherrer's equation [35], to be 12.7 and 15.1 nm for Py (50-nm) and Py (100-nm) films, respectively. These obtained values are very close to the values reported in the literature for polycrystalline Py thin films [36,37].

To film the qualities such as roughness, thickness, and average electron density of different sublayers of Sub/Py (50, 100)/SiO₂(5) thin films, we have measured the XRR spectra using an 8-keV x-ray source [as shown in Fig. 1(c)] and analyzed the spectra using GENX software [38]. The thicknesses obtained from the fit are close to the nominal thickness values. Average surface roughness obtained from the fit for 50- and 100-nm-thick films are 0.62 and 0.55 nm, respectively. Electron densities of Py and SiO₂ are found to be $7.1 \times 10^{-5} \text{Å}^{-2}$ and $2.0 \times 10^{-5} \text{Å}^{-2}$, respectively, in both the films. We have also measured the surface topography of

these films using AFM in dynamic tapping mode by taking scans over a $5 \times 5\text{-}\mu\text{m}^2$ area as shown in Fig. 1(d) for the 100-nm-thick film. Due to the thin capping layer, the interfacial roughness reflects its imprint on the topographical roughness. We have analyzed the AFM images using WSXM software [39]. The variation in surface roughness is found to be very small when measured at different regions of the same sample. Topographical roughness of 50- and 100-nm-thick films are found to be 0.86 and 0.80 nm, respectively, which are slightly higher than the values obtained from the XRR analyses possibly due to large area averaging.

B. Magnetization dynamics at different timescales

When a conventional ferromagnetic material is excited by a femtosecond laser pulse, its magnetization is partially or fully quenched in subpicosecond timescale, which is known as ultrafast demagnetization. This instantaneous quenching is followed by a faster recovery within few picoseconds and a slower recovery within hundreds of picoseconds, known as the fast and slow remagnetization, respectively. The slow remagnetization is accompanied by the damped sinusoidal precession in the presence of an external magnetic field triggered by an instantaneous change in the demagnetizing field

of the sample. The schematic of experimental geometry is shown in Fig. 1(e). Representative TR-MOKE data obtained from the 50-nm-thick Py film for $H = 2.40$ kOe and $F = 10$ mJ/cm² are shown in Fig. 1(f). There are three different temporal regimes, i.e., ultrafast demagnetization (region I), fast remagnetization (region II), and slow remagnetization with precession (region III). The red solid line in Fig. 1(f) is a fit to the exponential background originating from the heat diffusion during the slow relaxation process from the system to the surrounding.

C. Laser-induced ultrafast demagnetization

Since the discovery of ultrafast demagnetization in Ni thin film by Beaurepaire *et al.* in 1996 [14], several models have been proposed to interpret its origin [40–42]. Among those, the phenomenological three-temperature (3T) model has been widely used which deals with the energy exchange between the three heat baths, namely the electron, spin, and lattice baths. Upon laser excitation, electron temperature increases instantaneously to create a hot electron population above the Fermi level, which then triggers the quenching of magnetization in the spin subsystem by electron-magnon interaction. Subsequently, the energy rebalancing between these three subsystems ensures that the quenched magnetization relaxes back into its original equilibrium position. The temporal evolution of these three subsystems can be described by the following coupled differential equations [14,15,43,44]:

$$C_E(T_E) \frac{dT_E}{dt} = -G_{EL}(T_E - T_L) - G_{ES}(T_E - T_S) + \nabla_z(k\nabla_z T_E) + P(t), \quad (1)$$

$$C_S(T_S) \frac{dT_S}{dt} = -G_{ES}(T_S - T_E) - G_{SL}(T_S - T_L), \quad (2)$$

$$C_L(T_L) \frac{dT_L}{dt} = -G_{EL}(T_L - T_E) - G_{SL}(T_L - T_S), \quad (3)$$

where the temperatures of the electron, spin, and lattice baths are denoted by T_E , T_S , and T_L , respectively. C_E , C_S , and C_L are the electron, spin, and lattice specific heats. G_{EL} , G_{ES} , and G_{SL} are the electron-lattice, electron-spin, and spin-lattice coupling constants, respectively. $P(t)$ is the laser excitation term which is generally Gaussian in nature. The term $\nabla_z(k\nabla_z T_E)$ represents thermal diffusion, characterizing heat dissipation through thermal conduction across the sample's thickness (temporal and spatial evolutions of electronic heat diffusion for 50- and 100-nm Py films at pump fluence of 20 mJ/cm² are shown in Fig. S1 of the Supplemental Material [45]). Here, k stands for electronic thermal conductivity. The lattice (phonon) heat bath is assumed to have a much larger specific-heat capacity in comparison to the electron subsystem. Therefore, the heat diffusion is much faster through the electron heat bath as opposed to phonons, as proposed in the recent literature [44,46,47]. Thus, the lattice bath can absorb and store more energy without experiencing significant rise in temperature. Because of this, the lattice heat-diffusion term is neglected in our three-temperature modeling. This assumption simplifies the model and allows us to focus on the other dominant heat-transfer processes as suggested by several re-

cent studies [15,43,44,46–51]. Moreover, we have neglected the effect of heat diffusion to the substrate on the ultrafast demagnetization. Generally, the heat diffusion to substrate is more prominent in the presence of conducting substrates (that acts as an effective heat sink and affects the ultrafast demagnetization via superdiffusive spin-transport mechanism [19]) and very thin samples where substrate is directly excited by the laser pulse [43,52–54]. However, our sample thickness is much higher than that of the optical penetration depth and the Si substrate is coated with 285-nm-thick SiO₂ insulating layer. In our calculation, we have considered a linear contribution of the electronic specific heat, i.e., $C_E = \gamma T_E$, where γ is determined by the electron density of states around the Fermi level. Solving Eqs. (1)–(3) and subsequently by using mean-field theory, the magnetization of the system as a function of time can be extracted. The experimentally measured demagnetization curves can also be fitted with the following expression to extract the τ_m and τ_e directly [55,56]:

$$-\frac{\Delta M_z}{M_z} = \left[\left\{ \frac{A_1}{(t/\tau_0 + 1)^{1/2}} + \frac{A_1 \tau_m - A_2 \tau_e}{\tau_e - \tau_m} e^{-t/\tau_m} + \frac{A_2 \tau_e - A_1 \tau_e}{\tau_e - \tau_m} e^{-t/\tau_e} \right\} H(t) + A_3 \delta(t) \right] \otimes G(t). \quad (4)$$

In the above expression, A_1 represents the value of magnetization after equilibrium between electron, spin, and lattice is established; A_2 is proportional to the maximum rise in the electron temperature and A_3 represents the magnitude of state filling effect during pump-probe temporal overlap, well described by a Dirac-delta function $[\delta(t)]$. The cooling time by heat diffusion is described by τ_0 representing the timescale of electron-phonon interactions. $H(t)$ and $G(t)$ are the Heaviside step function and Gaussian function, respectively. The latter corresponds to the profile of the laser pulse. The two exponential terms in the above equation mirror the timescale of magnetization loss by the ultrafast demagnetization and the timescale of electron-phonon interaction by fast remagnetization of magnetization. The temporal changes of Kerr rotation $[\Delta\theta_k(t)]$ for all the measurements are normalized by the total Kerr rotation (θ_k) and then fitted with Eq. (4). Figures 2(a) and 2(b) show the laser-induced ultrafast demagnetization obtained at different laser pump fluence for Py thicknesses of 50 and 100 nm, respectively. We observe a monotonic increase in τ_m and τ_e with pump fluence for both films [Figs. 2(c) and 2(d)]. The enhancement in τ_m is an indication of the enhanced spin fluctuations at an elevated temperature of the spin system which may be due to an increase in dynamic longitudinal susceptibility and a decrease in exchange-interaction strength [57]. The increase in τ_e with pump fluence can be explained by the fact that there is an increase in the specific-heat capacity with laser fluence. The specific-heat capacity (energy required to increase the temperature of unit mass by 1 K) will influence this magnetization recovery process by affecting the temperature change that occurs during this process. With the increase in specific-heat capacity, a system absorbs more energy for a given temperature change. This means that the temperature change induced by laser pulse excitation will be smaller in higher specific-heat capacity states. As a result, the system will experience lower cooling rate during the re-

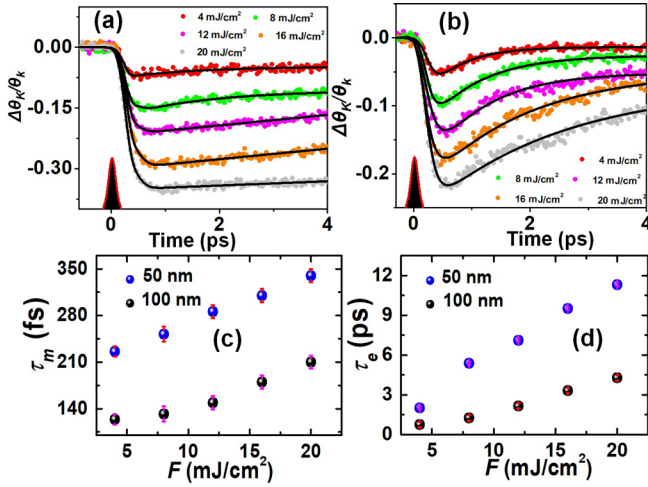


FIG. 2. Time-resolved Kerr rotation traces showing ultrafast demagnetization for (a) 50- and (b) 100-nm-thick Py film at different pump fluences. Symbols denote experimental data points and solid lines represent fitted curves using Eq. (4). Fluence-dependent variation of (c) ultrafast demagnetization time (τ_m) and (d) fast relaxation time (τ_e) obtained as fitting parameters.

magnetization process, leading to longer τ_e . At higher pump fluences, the cooling dynamics of both the electron and lattice systems exhibit notably slower behavior [58]. Also, higher fluence causes a greater rise in electron temperature followed by spin temperature and hence, magnetization takes more time for recovery to its initial equilibrium [59,60]. Under these circumstances at higher fluence, the remagnetization process slows down, leading to higher τ_e [57–60].

Also, we have observed that there is a continuous increase in A_1 and A_2 with pump fluence in these thin films due to higher quenching, longer thermal-relaxation time, and higher

increase in electron temperature at elevated fluence (shown in Tables S1 and S2). In our TR-MOKE measurements time-resolved transient reflectivity signal is captured in tandem with the Kerr rotation signal. Figure S2 of Supplemental Material [45] shows the transient reflectivity data at different laser fluences. The relative variation in Kerr rotation is about one to two orders of magnitude larger than the relative variation in transient reflectivity at any given fluence (as shown in Fig. S3 of Supplemental Material [45]). This rules out the possibility of the breakthrough of the nonmagnetic contributions to magnetic signal in highly excited states [61].

To explore the underlying physics involved in the ultrafast demagnetization process we have modeled the experimental demagnetization data using Eqs. (1)–(3). In this modeling, we have used $k = 90.7 \text{ Js}^{-1} \text{ m}^{-1} \text{ K}^{-1}$ and $\gamma = 5.05 \times 10^3 \text{ Jm}^{-3} \text{ K}^{-2}$ for Py (a weighted average of the values of iron and nickel). Figures 3(a) and 3(b) shows the temporal evolution of T_E , T_S , and T_L for 50- and 100-nm-thick Py films at $F = 20 \text{ mJ/cm}^2$. The values of specific heats and coupling constants for 50- and 100-nm-thick films are tabulated in Table I. The 100-nm-thick film has slightly higher C_L in comparison with the thinner 50-nm film. Using a model based on Debye-Einstein approximation, Alassafee *et al.* observed that with the increase of size of a system, C_L increases non-monotonically and eventually saturates in the bulk limit [62]. In their case, this increase in C_L with system size is primarily due to an increase in bulk modulus, isobaric linear thermal expansion, and Debye temperature, along with a reduction in the Grüneisen parameter (describes the dependence of the lattice vibration frequency on the relative change in volume or temperature). The 50-nm-thick Py film possesses lower values of G_{EL} , G_{ES} , and G_{SL} in comparison with 100-nm-thick Py. This observation corroborates the higher τ_m and τ_e values and indicates an easier energy dissipation in the thicker sample. This, in turn, signifies a larger increase in system temperature

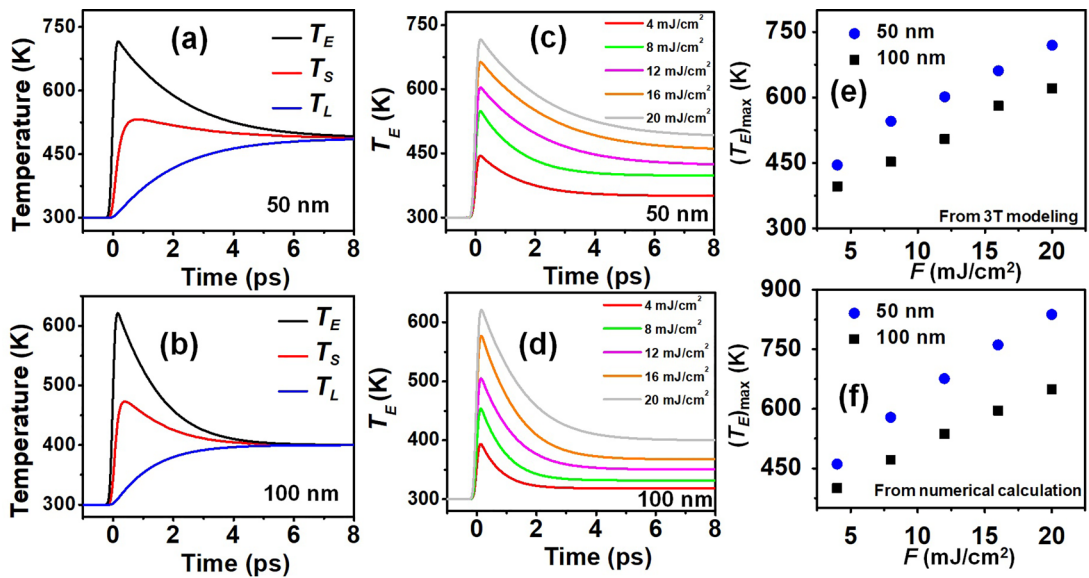


FIG. 3. Temporal evolution of electron temperature (T_E), spin temperature (T_S), and lattice temperature (T_L) for (a) 50-nm and (b) 100-nm Py film for pump fluence of 20 mJ/cm^2 . Variation of T_E as function of time delay at different laser pump fluence for (c) 50-nm and (d) 100-nm Py film. (e) Maximum electronic temperature rise $[(T_E)_{\max}]$ at different laser pump fluences obtained from 3T modeling. (f) $(T_E)_{\max}$ at different laser pump fluences calculated numerically using Eq. (5).

TABLE I. Parameters obtained from 3T modeling for 50- and 100-nm Py film.

Py thickness	Fluence (mJ/cm ²)	C_L (10 ⁶ Jm ⁻³ K ⁻¹)	C_S (10 ⁵ Jm ⁻³ K ⁻¹)	G_{EL} (10 ¹⁷ Wm ⁻³ K ⁻¹)	G_{ES} (10 ¹⁷ Wm ⁻³ K ⁻¹)	G_{SL} (10 ¹⁷ Wm ⁻³ K ⁻¹)
50 nm	4	4.21	2.13	9.53	6.01	5.20
	8	4.23	2.19	9.51	6.82	5.22
	12	4.40	2.27	6.03	6.01	5.21
	16	4.48	2.33	6.28	5.14	4.95
	20	4.53	2.34	5.51	4.02	4.92
	4	6.65	2.10	18.04	14.01	8.60
100 nm	8	6.71	2.17	16.07	12.02	8.69
	12	6.78	2.23	12.71	11.91	7.73
	16	6.80	2.24	13.00	11.04	7.71
	20	6.84	2.26	9.05	10.18	8.64

in thinner films in comparison with the thicker films within a comparable fluence range.

Furthermore, we observed an increase in both C_L and C_S as laser fluence increases, which may be attributed to a corresponding rise in their respective bath temperatures. This increase in specific-heat capacities will also make the magnetization recovery process slower by slowing down the temperature change that occurs during this process. With the increased heat capacity, the system will require more energy for a unit temperature change. As a result, it will experience lower cooling rate during remagnetization process, leading to larger τ_c . In contrast, G_{ES} and G_{EL} exhibit a decrease with laser fluence while G_{SL} shows a negligible change. Recent literature indicates an inverse relationship between that ultrafast demagnetization time and G_{ES} , which supports our observation [63]. A reduction in G_{EL} at higher fluence signifies a weakening electron-lattice coupling, leading to a longer time taken for electrons to attain equilibrium. In ferromagnetic transition metals, energy transfer between electrons and lattice dominates over that between spins and lattice [64]. This points to a limited impact of G_{SL} in the context of 3T modeling [43].

Figures 3(c) and 3(d) show the temporal evolution of T_E for 50- and 100-nm-thick Py films at different laser pump fluences. Variation in maximum electronic temperature rise ($(T_E)_{\max}$) from this modeling is plotted in Fig. 3(e), which confirms the continuous increase in electronic temperature with laser fluence. We will now compare this electronic temperature rise with some theoretical arguments, where the $(T_E)_{\max}$ is related to the peak absorbed laser energy per unit volume (E_a) by the following relation [65]:

$$(T_E)_{\max} = \sqrt{\frac{2E_a}{\gamma} + T_0^2}, \quad \text{where} \quad E_a = [1 - e^{-d/\lambda}] \frac{F(1-R)}{d}, \quad (5)$$

where d is the film thickness, λ is the optical penetration depth (~ 17 nm), R is the reflectivity of the sample (~ 0.5), and T_0 is the ambient temperature (~ 300 K for room temperature). Variation in T_E with laser pump fluence for both the films using the expression in Eq. (5) is plotted in Fig. 3(f). T_E derived from the numerical calculation shows qualitative agreement with that obtained using the 3T modeling. Similar to T_E , there is also an increase in T_S and T_L with the laser fluences (as shown in Fig. S4 and S5 of the Supplemental Material [45]).

The highest temperature attained by spin bath is much lower than the Curie temperature (~ 863 K for Py [66]). Hence, we have excluded any additional heat capacity for the spin system in our 3T modeling analysis [67].

D. Laser-induced modulation of precessional dynamics

The precession of magnetization around an effective magnetic field appears as a damped sinusoidal oscillation in the time-resolved Kerr rotation data in the picosecond to nanosecond timescale. We have extracted the precessional relaxation time (τ) by fitting the background-subtracted Kerr oscillations using the following expression [66,68]:

$$M(t) = \sum_i A_i e^{-(t/\tau_i)} \sin(2\pi (f_i + b_i t)t + \phi_i), \quad (6)$$

where A_i , τ_i , f_i , ϕ_i , and b_i are, respectively, the precessional amplitude, relaxation time, precessional frequency, initial phase, and temporal chirp parameter for the i th mode. For all these samples we have investigated the precessional dynamics at various H values. The fast Fourier transformation (FFT) of the oscillations provides f_i for different values of H . The field dispersion of frequency (f) is fitted using the following expression [69]:

$$f = \frac{\gamma}{4\pi} \sqrt{\left(H + \frac{2A}{M_s} \left(\frac{n\pi}{d}\right)^2\right) \left(H + \frac{2A}{M_s} \left(\frac{n\pi}{d}\right)^2 + 4\pi M_{\text{eff}}\right)}, \quad (7)$$

where M_{eff} is effective magnetization and $\gamma (= g\mu_B/\hbar)$ is the gyromagnetic ratio. g and \hbar are the Landé g factor and reduced Planck's constant, respectively. Here, A , n , and d are the exchange-stiffness constant, order of PSSW mode, and thickness of the film, respectively. For uniform Kittel mode $n = 0$, while $n = 1$ and 2 stand for first- and second-order PSSW mode. The A value is taken from the literature [70] as 1.3×10^{-6} erg/cm for Py. M_{eff} and g are determined as the fitting parameters here. After finding τ and M_{eff} , we have estimated the effective damping, α using the following expression [71]:

$$\alpha = \frac{1}{\gamma\tau(H + 2\pi M_{\text{eff}})}, \quad (8)$$

where the value of γ is 1.76×10^7 Hz/Oe. Figures 4(a) and 4(b) show the time-resolved Kerr oscillations for differ-

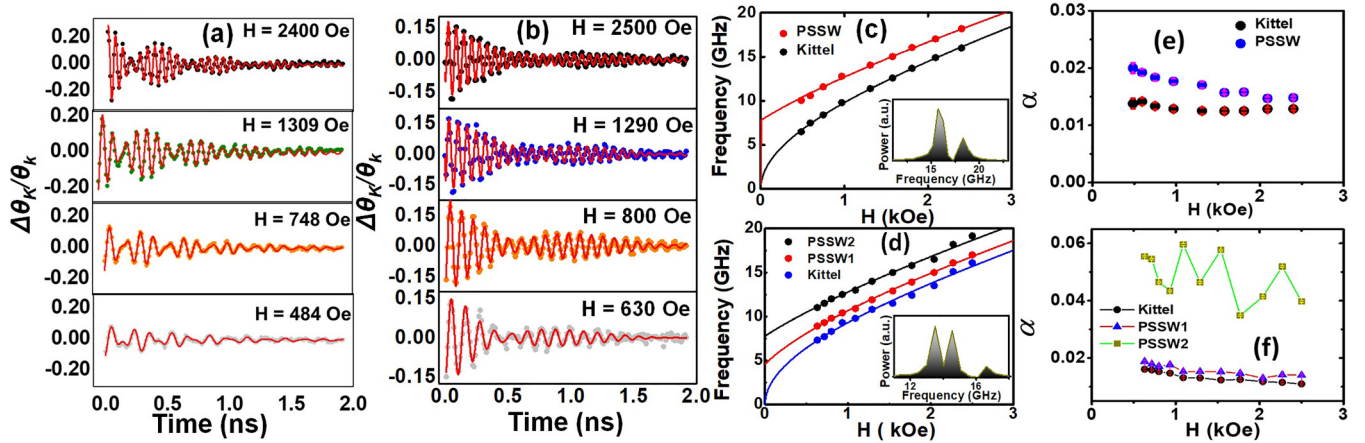


FIG. 4. Background-subtracted time-resolved Kerr rotation data showing precessional oscillations at different bias magnetic field(H) values for (a) 50-nm and (b) 100-nm-thick Py film. Symbols represent experimental data points and solid lines represent fit using Eq. (6). Precessional frequency as function of H (symbols) and corresponding Kittel fit (solid line) for (c) 50-nm and (d) 100-nm-thick Py film is shown. [Insets show the fast Fourier transformation power spectra at the highest field which clearly shows (c) two modes for 50-nm-thick Py film and (d) three modes for 100-nm-thick Py film]. Gilbert damping parameter (α) as function of H for (e) 50-nm and (f) 100-nm-thick Py film.

ent bias magnetic fields at $F = 10 \text{ mJ/cm}^2$ for the 50- and 100 nm-thick Py film, respectively. Figures 4(c) and 4(d) show the f vs H plot fitted with the Kittel formula in Eq. (7) for 50- and 100-nm-thick Py film, respectively. There are two modes for the 50-nm-thick film [as shown in the inset of Fig. 4(c)]: one corresponding to the uniform Kittel mode with lower frequency and the other corresponding to first-order PSSW mode with higher frequency, whereas three clear modes appear for the 100-nm-thick film [as shown in the inset of Fig. 4(d)]: a low-frequency uniform Kittel mode and first- and second-order PSSW modes. From the Kittel fit, we have obtained $M_{\text{eff}} \approx 790 \pm 10 \text{ emu/cc}$ and $g = 2.0 \pm 0.1$ for the Kittel and the PSSW modes of both Py films, which are close to the values obtained from VSM ($\sim 800 \text{ emu/cc}$). The amplitude of precession is found to increase with H (as shown in Figs. S6 and S7 of Supplemental Material [45]), which can be attributed to the enhancement of INP magnetization component with increasing magnetic field strength. With the increase in H , there is an increase in magnetic torque ($M \times H_{\text{eff}}$ term in Landau-Lifshitz-Gilbert equation) which prefers a large angle between M and H_{eff} , leading to higher precessional amplitude [72,73]. Increase in OOP magnetic field can also increase the precessional amplitude in TR-MOKE measurement, leading to higher canting angle of magnetization with respect to the sample plane prior to optical excitation. However, in our measurement setup, we have maintained the initial OOP canting at a constant value to ensure it does not exert varying impacts on the precessional amplitude when altering laser fluence and magnetic field strength. α is found to be independent of H [as shown in Figs. 4(e) and 4(f)]. The literature shows that in the presence of extrinsic effects like two-magnon scattering, α decreases with the applied magnetic field due to the increased degeneracy of spin waves while it should increase in the presence of inhomogeneous surface anisotropy [22]. A field-independent nature of α rules out the presence of any such extrinsic contributions in our system.

To study the effect of laser pump fluence (F) on precessional dynamics, we have varied F from 4 to 20 mJ/cm^2 at $H = 2.4 \text{ kOe}$. The precessional data at different pump fluences for 50- and 100-nm-thick Py are plotted in Figs. 5(a) and 5(b), respectively. The amplitude of precession increases with F (as shown in Fig. S6 and S7 of Supplemental Material [45]) due to the stronger modulation of magnetization and the effective field. The variation of α with F is plotted in Figs. 5(c) and 5(d) for 50- and 100 nm-thick Py films, which shows damping increases significantly from its intrinsic value for both Kittel and PSSW modes within this fluence range. We have observed that damping of Kittel and PSSW modes is following the similar increasing trend with laser fluence. This trend signifies that there is no intermode energy transfer between different modes [68]. Although there is a finite possibility of laser fluence-induced damping enhancement due to the eddy current and nonlocal contribution from the propagation of magnetostatic spin waves, recent studies show that eddy-current contribution in Py films below 100 nm is negligible [74] and nonlocal contribution to damping is more significant when the excitation area is below $10 \mu\text{m}$ [75]. Throughout the measurement we have carefully maintained the overlap between the probe and pump beams and the Kerr signal is collected from the uniformly excited region with a $100\text{-}\mu\text{m}$ spot size. Thus, the introduction of any nonlocal effects is very unlikely. Among various other mechanisms responsible for the laser fluence-induced damping, the spin-lattice interaction mechanism can be a dominant one. In the presence of this mechanism, energy density deposited in the probed volume increases with laser fluence, which causes an enhancement in the energy dissipation from the spin system to lattice, which in turn accelerates the decay of spin waves. We have observed that lattice temperatures (extracted from the 3T modeling) for the 50- and 100-nm-thick films increase from approximately 350.7 to 485.2 K and 318.6 to 399.7 K within the experimental fluence range (as shown in Fig. S5

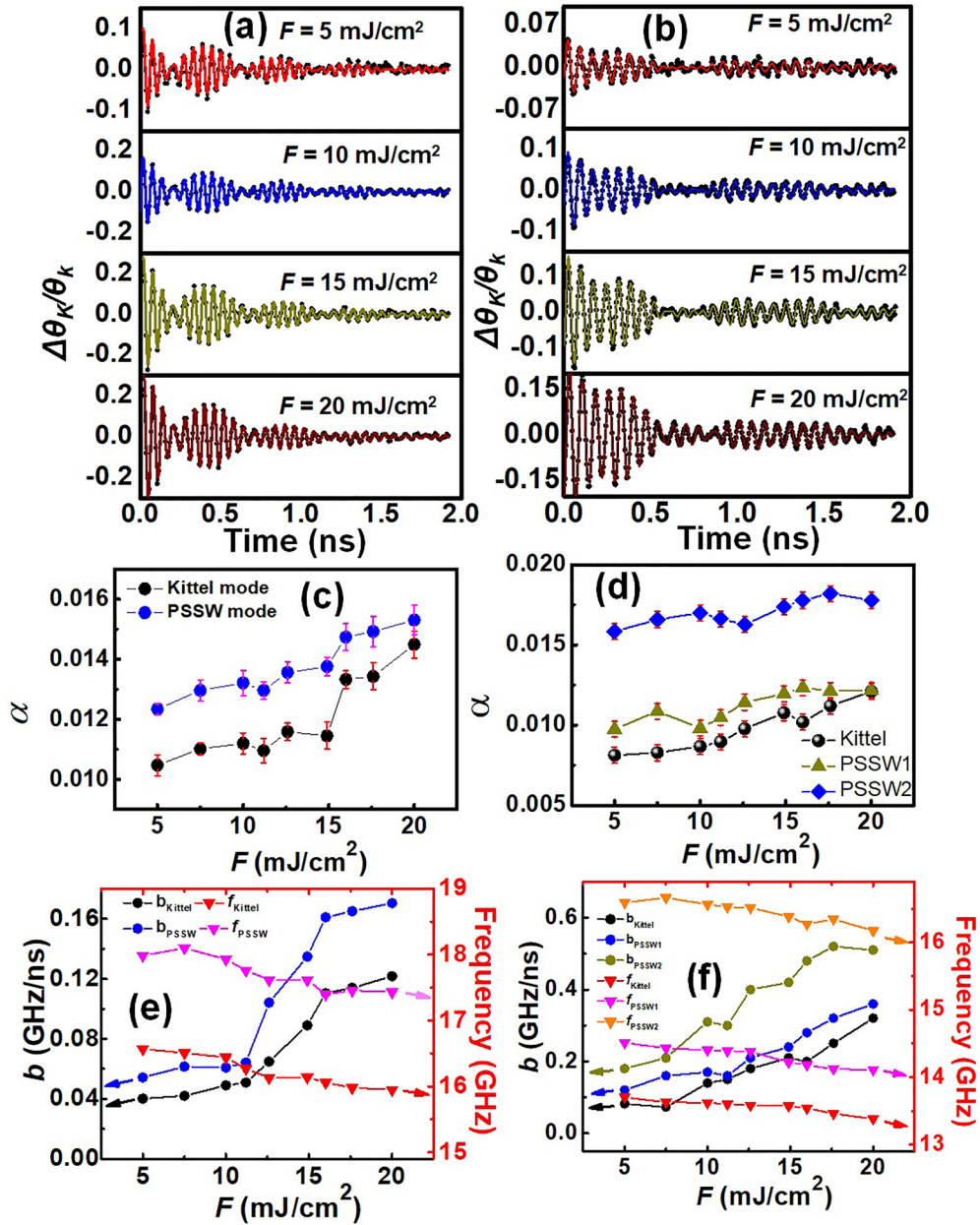


FIG. 5. Background-subtracted time-resolved Kerr rotation data showing precessional dynamics at different laser pump fluence (F) for (a) 50-nm and (b) 100-nm Py film. Symbols represent experimental data points and solid lines represent fit using Eq. (6). Variation of Gilbert damping parameter (α) with laser fluence for (c) 50-nm and (d) 100-nm Py film. Precessional frequency and temporal chirp parameter as function of laser fluence for (e) 50-nm and (f) 100-nm Py film.

of Supplemental Material [45]). As α is proportional to the susceptibility of the sample, which is a function of the lattice temperature, any change in the lattice temperature with laser fluence will affect α . According to the Landau-Lifshitz-Bloch model, an increase in the laser fluence will increase the ratio between the system temperature and Curie temperature, which induces electron-impurity led spin-dependent scattering and causes the enhancement of α [76]. The possibility of irreversible damage in the probed area due to high fluence cannot be ignored. To verify this, we have performed another set of experiments where the probed area is exposed to different irradiation pump fluences (F_i) for 15 min. After the irradiation,

the precessional dynamics is measured from that area with a low pump fluence of 4 mJ/cm^2 . We find that precessional frequency and damping remain almost invariant for all the irradiation fluences up to 20 mJ/cm^2 (as shown in Fig. S8 of Supplemental Material [45]). These results demonstrate that pump-induced modification of the magnetization dynamics is reversible and transient in nature within our experimental fluence range.

With an increase in the pump fluence, precessional frequencies of both the Kittel and the PSSW modes show considerable redshift [as shown in Figs. 5(e) and 5(f), respectively]. The frequencies of Kittel and first-order PSSW

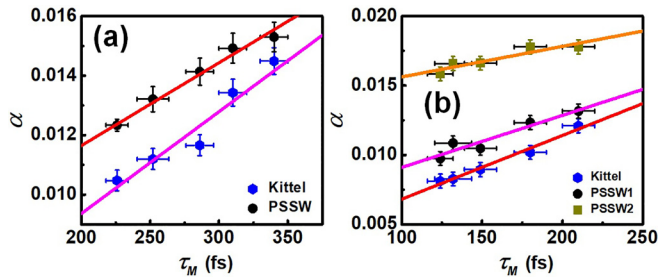


FIG. 6. Gilbert damping parameter (α) as function of ultrafast demagnetization time (τ_m) for (a) 50-nm and (b) 100-nm Py thin films. Solid line is linear fit to data.

modes in the 50-nm-thick film are reduced by 3.41 and 4.60%. For the 100-nm-thick film, the frequencies of Kittel and first- and second-order PSSW modes are reduced by 2.33, 2.78, and 3.24%, respectively. This decrease in frequency is mainly due to a change in the local magnetic properties such as magnetic moment, susceptibility, anisotropy, etc., by rapid accumulation and dissipation of thermal energy in the probed volume, which introduces temporal chirping [66,77]. Chirping appears in a time-dependent Kerr oscillation signal because with passing time magnetization of the sample acquires an equilibrium state but the precessional frequency is unable to attain a stable equilibrium state and continues to change. The temporal chirp parameter (b) shows negligible dependence on the bias magnetic field as plotted in Fig. S9 of Supplemental Material [45]. However, it increases significantly with the laser pump fluence for both 50- and 100-nm-thick films as shown in Figs. 5(e) and 5(f), respectively. Enhancement in b for the PSSW modes is higher in comparison with that of the uniform Kittel mode, which implies higher-frequency modulation of these bulk modes due to the nonuniform distribution of heat across the thickness of the magnetic layer.

The correlation between τ_m and α is of significant interest in recent times, as it is an effective method to detect the governing microscopic contribution to ultrafast demagnetization and damping [20–23,78,79]. According to this, a proportional relationship between the τ_m and α indicates that the local spin-flip scattering mechanism dominates the demagnetization process. However, an inverse dependence implies that the nonlocal spin-transport mechanism dominates the demagnetization process. By plotting τ_m with α for 50- and 100-nm-thick Py films obtained at different pump fluences in Figs. 6(a) and 6(b), we have observed an increase in τ_m with α . This proportional relationship signifies that spin-flip scattering is the dominant microscopic mecha-

nism for ultrafast demagnetization in our system. Also, the correlation between τ_m and α helps to determine the major microscopic contribution to the damping. A linear relationship points to the dominance of intraband conductivity-like contribution, whereas an inverse relationship indicates the interband resistivity-like contribution. Hence, the observed linear relationship between τ_m and α signifies that intraband conductivity-like contribution dominates the damping process in our samples.

IV. CONCLUSION

An extensive and systematic study of ultrafast magnetization dynamics is presented for 50- and 100-nm-thick Py thin films at different pump fluences and bias magnetic field by an all-optical TR-MOKE magnetometry. A strong correlation between the ultrafast demagnetization time and fast remagnetization time with the pump fluence is observed. The Gilbert damping parameter for both Kittel and perpendicular standing spin-wave modes remains independent of applied bias magnetic field while showing significant enhancement from intrinsic value with an increase in the pump fluence. The precessional frequencies experience a noticeable redshift with pump fluence due to a change in the accumulation and dissipation of thermal energy in the probed area, leading to a temporal chirping. A direct relationship between τ_m and α is established due to the dominant spin-flip scattering contribution to ultrafast demagnetization and intraband conductivity-like contribution to damping for Py films. This elaborative study will enlighten the understanding of the modulation of magnetization dynamics in ferromagnetic systems in the presence of different external conditions and helps in optimizing parameters for spin-based devices in accordance with external conditions.

ACKNOWLEDGMENTS

A.B. gratefully acknowledges the financial assistance from the S. N. Bose National Centre for Basic Sciences (SNBNCBS), India under Projects No. SNB/AB/11–12/96 and No. SNB/AB/18–19/211.

A.B. planned and supervised the project; S. Majumder grew the thin films; S. Mondal and S.N.P. performed the time-resolved MOKE measurements and data analyses in consultation with A.B.; and S.N.P. and A.B. wrote the manuscript. All authors contributed to the discussion and editing of the manuscript.

The authors declare no competing financial interest.

- [1] I. Zutic, J. Fabian, and S. Das Sharma, Spintronics: Fundamentals and applications, *Rev. Mod. Phys.* **76**, 323 (2004).
- [2] S. A. Wolf, D. D. Awschalom, R. A. Buhrman, J. M. Daughton, S. von Molnar, M. L. Roukes, A. Y. Chtchelkanova, and D. M. Treger, Spintronics: A spin-based electronics vision for the future, *Science* **294**, 1488 (2001).
- [3] A. Hoffmann and S. D. Bader, Opportunities at the frontiers of spintronics, *Phys. Rev. Appl.* **4**, 047001 (2015).

- [4] S. D. Bader and S. S. P. Parkin, Spintronics, *Annu. Rev. Cond. Matter Phys.* **1**, 71 (2010).
- [5] L. Landau and E. Lifshitz, On the theory of the dispersion of magnetic permeability in ferromagnetic bodies, *Phys. Z. Sowjet.* **8**, 153 (1935).
- [6] T. L. Gilbert, A phenomenological theory of damping in ferromagnetic materials, *IEEE Trans. Magn.* **40**, 3443 (2004).

- [7] A. Barman and J. Sinha, *Spin Dynamics and Damping in Ferromagnetic Thin Films and Nanostructures* (Springer, Switzerland, 2018).
- [8] P. He, X. Ma, J. W. Zhang, H. B. Zhao, G. Lüpke, Z. Shi, and S. M. Zhou, Quadratic scaling of intrinsic Gilbert damping with spin-orbital coupling in $L1_0\text{FePdPt}$ films: Experiments and *ab initio* calculations, *Phys. Rev. Lett.* **110**, 077203 (2013).
- [9] P. Krivosik, N. Mo, S. Kalarickal, and C. E. Patton, Hamiltonian formalism for two magnon scattering microwave relaxation: Theory and applications, *J. Appl. Phys.* **101**, 083901 (2007).
- [10] J. O. Rantschler, R. D. McMichael, A. Castillo, A. J. Shapiro, W. F. Egelhoff, B. B. Maranville, D. Pulugurtha, A. P. Chen, and L. M. Connors, Effect of $3d$, $4d$ and $5d$ transition metal doping on damping in permalloy thin films, *J. Appl. Phys.* **101**, 033911 (2007).
- [11] Y. Tserkovnyak, A. Brataas, and G. E. W. Bauer, Spin pumping and magnetization dynamics in metallic multilayers, *Phys. Rev. B* **66**, 224403 (2002).
- [12] Y. Zhao, Q. Song, S. H. Yang, T. Su, W. Yuan, S. S. P. Parkin, J. Shi, and W. Han, Experimental investigation of temperature-dependent Gilbert damping in permalloy thin films, *Sci. Rep.* **6**, 22890 (2016).
- [13] A. Ganguly, R. M. Rowan-Robinson, A. Haldar, S. Jaiswal, J. Sinha, A. T. Hindmarch, D. A. Atkinson, and A. Barman, Time-domain detection of current controlled magnetization damping in $\text{Pt}/\text{Ni}_{81}\text{Fe}_{19}$ bilayer and determination of Pt spin Hall angle, *Appl. Phys. Lett.* **105**, 112409 (2014).
- [14] E. Beaurepaire, J. C. Merle, A. Daunois, and J. Y. Bigot, Ultrafast spin dynamics in ferromagnetic nickel, *Phys. Rev. Lett.* **76**, 4250 (1996).
- [15] B. Koopmans, G. Malinowski, F. Dalla Longa, D. Steiauf, M. Fähnle, T. Roth, M. Cinchetti, and M. Aeschlimann, Explaining the paradoxical diversity of ultrafast laser-induced demagnetization, *Nat. Mater.* **9**, 259 (2010).
- [16] J. Y. Bigot, M. Vomir, and E. Beaurepaire, Coherent ultrafast magnetism induced by femtosecond laser pulses, *Nat. Phys.* **5**, 515 (2009).
- [17] M. Krauß, T. Roth, S. Alebrand, D. Steil, M. Cinchetti, M. Aeschlimann, and H. C. Schneider, Ultrafast demagnetization of ferromagnetic transition metals, *Phys. Rev. B* **80**, 180407(R) (2009).
- [18] G. P. Zhang, W. Hubner, G. Lefkidis, Y. Bai, and T. F. George, Paradigm of the time-resolved magneto-optical Kerr effect for femtosecond magnetism, *Nat. Phys.* **5**, 499 (2009).
- [19] M. Battiato, K. Carva, and P. M. Oppeneer, Superdiffusive spin transport as a mechanism of ultrafast demagnetization, *Phys. Rev. Lett.* **105**, 027203 (2010).
- [20] B. Koopmans, J. J. M. Ruigrok, F. Dalla Longa, and W. J. M. de Jonge, Unifying ultrafast magnetization dynamics, *Phys. Rev. Lett.* **95**, 267207 (2005).
- [21] W. Zhang, W. He, X. Q. Zhang, Z. H. Cheng, J. Teng, and M. Fähnle, Unifying ultrafast demagnetization and intrinsic Gilbert damping in Co/Ni bilayers with electronic relaxation near the Fermi surface, *Phys. Rev. B* **96**, 220415(R) (2017).
- [22] W. Zhang, Q. Liu, Z. Yuan, K. Xia, W. He, Q. F. Zhan, X. Q. Zhang, and Z. H. Cheng, Enhancement of ultrafast demagnetization rate and Gilbert damping driven by femtosecond laser-induced spin currents in $\text{Fe}_{81}\text{Ga}_{19}/\text{Ir}_{20}\text{Mn}_{80}$ bilayers, *Phys. Rev. B* **100**, 104412 (2019).
- [23] M. Fähnle, J. Seib, and C. Illg, Relating Gilbert damping and ultrafast laser-induced demagnetization, *Phys. Rev. B* **82**, 144405 (2010).
- [24] A. Haldar, C. Banerjee, P. Laha, and A. Barman, Brillouin light scattering study of spin waves in NiFe/Co exchange spring bilayer films, *J. Appl. Phys.* **115**, 133901 (2014).
- [25] A. Conca, E. Th. Papaioannou, S. Klingler, J. Greser, T. Sebastian, B. Leven, J. Lösch, and B. Hillebrands, Annealing influence on the Gilbert damping parameter and the exchange constant of CoFeB thin films, *Appl. Phys. Lett.* **104**, 182407 (2014).
- [26] M. A. W. Schoen, J. M. Shaw, H. T. Nembach, M. Weiler, and T. J. Silva, Radiative damping in waveguide-based ferromagnetic resonance measured via analysis of perpendicular standing spin waves in sputtered permalloy films, *Phys. Rev. B* **92**, 184417 (2015).
- [27] T. Seki, K. Utsumiya, Y. Nozaki, H. Imamura, and K. Takanashi, Spin wave-assisted reduction in switching field of highly coercive iron-platinum magnets, *Nat. Commun.* **4**, 1726 (2013).
- [28] S. N. Panda, S. Mondal, J. Sinha, S. Choudhury, and A. Barman, All-optical detection of interfacial spin transparency from spin pumping in $\beta\text{-Ta}/\text{CoFeB}$ thin films, *Sci. Adv.* **5**, eaav7200 (2019).
- [29] A. Kirilyuk, A. V. Kimel, and T. Rasing, Ultrafast optical manipulation of magnetic order, *Rev. Mod. Phys.* **82**, 2731 (2010).
- [30] H. D. Arnold and G. W. Elmen, Permalloy, a new magnetic material of very high permeability, *Bell Syst. Tech. J.* **2**, 101 (1923).
- [31] M. van Kampen, C. Jozsa, J. T. Kohlhepp, P. LeClair, L. Lagae, W. J. M. de Jonge, and B. Koopmans, All-Optical probe of coherent spin waves, *Phys. Rev. Lett.* **88**, 227201 (2002).
- [32] F. Bohn, M. A. Corrêa, A. Da Cas Viegas, S. Papanikolaou, G. Durin, and R. L. Sommer, Universal properties of magnetization dynamics in polycrystalline ferromagnetic films, *Phys. Rev. E* **88**, 032811 (2013).
- [33] T. Ohtani, T. Kawai, M. Ohtake, and M. Futamoto, Magnetostriction of permalloy epitaxial and polycrystalline thin films, *EPJ Web Conf.* **40**, 11004 (2013).
- [34] A. Guittoum, A. Bourzami, A. Layadi, and G. Schmerber, Structural, electrical and magnetic properties of evaporated permalloy thin films: Effect of substrate and thickness, *Eur. Phys. J. Appl. Phys.* **58**, 20301 (2012).
- [35] J. I. Langford and A. Wilson, Scherrer after sixty years: A survey and some new results in the determination of crystallite size, *J. Appl. Crystallogr.* **11**, 102 (1978).
- [36] R. Gupta and M. Gupta, Nanocrystallization and amorphization induced by reactive nitrogen sputtering in iron and permalloy, *Phys. Rev. B* **72**, 024202 (2005).
- [37] J. Park, H. Ko, J. Kim, J. Park, S. Park, Y. Jo, B. Park, S. K. Kim, K. Lee, and K. Kim, Temperature dependence of intrinsic and extrinsic contributions to anisotropic magnetoresistance, *Sci. Rep.* **11**, 20884 (2021).
- [38] A. Glavic and M. Bjorck, GenX3: The latest generation of an established tool, *J. Appl. Crystallogr.* **55**, 1063 (2022).
- [39] I. Horcas, R. Fernández, J. M. Gómez-Rodríguez, J. Colchero, J. Gómez-Herrero, and A. M. Baro, WSXM: A software for scanning probe microscopy and a tool for nanotechnology, *Rev. Sci. Instrum.* **78**, 013705 (2007).

- [40] B. Koopmans, H. H. J. E. Kicken, M. van Kampen, and W. J. M. de Jonge, Microscopic model for femtosecond magnetization dynamics, *J. Magn. Magn. Mater.* **286**, 271 (2005).
- [41] A. Mekonnen, A. R. Khorsand, M. Cormier, A. V. Kimel, A. Kirilyuk, A. Hrabec, L. Ranno, A. Tsukamoto, A. Itoh, and Th. Rasing, Role of the inter-sublattice exchange coupling in short-laser-pulse-induced demagnetization dynamics of GdCo and GdCoFe alloys, *Phys. Rev. B* **87**, 180406(R) (2013).
- [42] S. I. Anisimov, B. L. Kapeliovitch, and T. L. Perel'man, Electron emission from metal surfaces exposed to ultrashort laser pulses, *Zh. Eksp. Teor. Fis.* **66**, 776 (1974).
- [43] S. Mukhopadhyay, S. Majumder, S. N. Panda, and A. Barman, Investigation of ultrafast demagnetization and Gilbert damping and their correlation in different ferromagnetic thin films grown under identical conditions, *Nanotechnology* **34**, 235702 (2023).
- [44] L. Jiang and H. Tsai, Improved two-temperature model and its application in ultrashort laser heating of metal films, *J. Heat Transfer* **127**, 1167 (2005).
- [45] See Supplemental Material at <http://link.aps.org/supplemental/10.1103/PhysRevB.108.144421> for (a) electronic heat-diffusion profile extracted using three-temperature modeling, (b) variation of transient reflectivity and Kerr rotation with pump fluence, (c) evolution of the spin and lattice temperatures with laser pump fluences, (d) evolution of FFT power spectra and its amplitude, (e) variation of precessional dynamics with irradiation fluence, and (f) variation of temporal chirp parameter with bias magnetic field.
- [46] R. H. M. Groeneveld, R. Sprik, and A. Lagendijk, Femtosecond spectroscopy of electron-electron and electron-phonon energy relaxation in Ag and Au, *Phys. Rev. B* **51**, 11433 (1995).
- [47] E. Carpane, Ultrafast laser irradiation of metals: Beyond the two-temperature model, *Phys. Rev. B* **74**, 024301 (2006).
- [48] M. Lisowski, P. A. Loukakos, U. Bovensiepen, J. Stähler, C. Gahl, and M. Wolf, Ultrafast dynamics of electron thermalization, cooling and transport effects in Ru(001), *Appl. Phys. A: Mater. Sci. Process.* **78**, 165 (2004).
- [49] R. Li, O. A. Ashour, J. Chen, H. E. Elsayed-Ali, and P. M. Rentzepis, Femtosecond laser induced structural dynamics and melting of Cu (111) single crystal. An ultrafast time-resolved x-ray diffraction study, *J. Appl. Phys.* **121**, 055102 (2017).
- [50] A. Nicarel, M. Oane, I. N. Mihailescu, and C. Ristoscu, Fourier two-temperature model to describe ultrafast laser pulses interaction with metals: A novel mathematical technique, *Phys. Lett. A* **392**, 127155 (2021).
- [51] S. I. Anisimov, B. L. Kapeliovich, and L. T. Perel'man, Electron emission from metal surfaces exposed to ultrashort laser pulses, *Sov. Phys. JETP* **9**, 375 (1974).
- [52] M. Battiato, K. Carva, and P. M. Oppeneer, Theory of laser-induced ultrafast superdiffusive spin transport in layered heterostructures, *Phys. Rev. B* **86**, 024404 (2012).
- [53] I. Razdolski, A. Alekhin, U. Martens, D. Bürstel, D. Diesing, M. Münzenberg, U. Bovensiepen, and A. Melnikov, Analysis of the time-resolved magneto-optical Kerr effect for ultrafast magnetization dynamics in ferromagnetic thin films, *J. Phys.: Condens. Matter* **29**, 174002 (2017).
- [54] F. Hoveyda, M. Adnani, and S. Smadici, Heat diffusion in magnetic superlattices on glass substrates, *J. Appl. Phys.* **122**, 184304 (2017).
- [55] F. Dalla Longa, J. T. Kohlhepp, W. J. M. de Jonge, and B. Koopmans, Influence of photon angular momentum on ultrafast demagnetization in nickel, *Phys. Rev. B* **75**, 224431 (2007).
- [56] G. Malinowski, F. Dalla Longa, J. H. H. Rietjens, P. V. Paluskar, R. Huijink, H. J. M. Swagten, and B. Koopmans, Control of speed and efficiency of ultrafast demagnetization by direct transfer of spin angular momentum, *Nat. Phys.* **4**, 855 (2008).
- [57] J. Mendil, P. Nieves, O. Chubykalo-Fesenko, J. Walowski, T. Santos, S. Pisana, and M. Münzenberg, Resolving the role of femtosecond heated electrons in ultrafast spin dynamics, *Sci. Rep.* **4**, 3980 (2014).
- [58] U. Atxitia, O. Chubykalo-Fesenko, J. Walowski, A. Mann, and M. Münzenberg, Evidence for thermal mechanisms in laser-induced femtosecond spin dynamics, *Phys. Rev. B* **81**, 174401 (2010).
- [59] M. R. Karim, A. Adhikari, S. N. Panda, P. Sharangi, S. Kayal, G. Manna, P. S. A. Kumar, S. Bedanta, A. Barman, and I. Sarkar, Ultrafast spin dynamics of electrochemically grown Heusler alloy films, *J. Phys. Chem. C* **125**, 10483 (2021).
- [60] S. N. Panda, B. Rana, Y. Otani, and A. Barman, Role of spin-orbit coupling on ultrafast spin dynamics in nonmagnet/ferromagnet heterostructures, *Adv. Quantum Technol.* **5**, 2200016 (2022).
- [61] E. Carpane, F. Boschini, H. Hedayat, C. Piovera, C. Dallera, E. Puppini, M. Mansurova, M. Münzenberg, X. Zhang, and A. Gupta, Measurement of the magneto-optical response of Fe and CrO₂ epitaxial films by pump-probe spectroscopy: Evidence for spin-charge separation, *Phys. Rev. B* **87**, 174437 (2013).
- [62] A. K. Alassafee and M. S. Omar, Debye-Einstein approximation approach to calculate the lattice specific heat and related parameters for a Si nanowire, *J. Tai. Uni. Sci.* **11**, 1226 (2017).
- [63] S. Pan, F. Ganss, S. Panda, G. Sellge, C. Banerjee, J. Sinha, O. Hellwig, and Anjan Barman, Mechanism of femtosecond laser induced ultrafast demagnetization in ultrathin film magnetic multilayers, *J. Mater. Sci.* **57**, 6212 (2022).
- [64] P.-W. Ma, S. L. Dudarev, and C. H. Woo, Spin-lattice-electron dynamics simulations of magnetic materials, *Phys. Rev. B* **85**, 184301 (2012).
- [65] E. Carpane, E. Mancini, C. Dallera, M. Brenna, E. Puppini, and S. De Silvestri, Dynamics of electron-magnon interaction and ultrafast demagnetization in thin iron films, *Phys. Rev. B* **78**, 174422 (2008).
- [66] S. Mondal and A. Barman, Laser controlled spin dynamics of ferromagnetic thin film from femtosecond to nanosecond timescale, *Phys. Rev. Appl.* **10**, 054037 (2018).
- [67] P. D. Desai, Thermodynamic properties of nickel, *Int. J. Thermophys.* **8**, 763 (1987).
- [68] S. Mondal, A. Talapatra, J. Arout Chelvane, J. R. Mohanty, and A. Barman, Role of magnetic anisotropy in the ultrafast magnetization dynamics of Gd-Fe thin films of different thicknesses, *Phys. Rev. B* **100**, 054436 (2019).
- [69] C. Banerjee, A. K. Chaurasiya, S. Saha, J. Sinha, and A. Barman, Tunable spin wave properties in [Co/Ni₈₀Fe₂₀]_r multilayers with the number of bilayer repetition, *J. Phys. D: Appl. Phys.* **48**, 395001 (2015).
- [70] C. Banerjee, S. Saha, S. Barman, O. Rousseau, Y. Otani, and A. Barman, Width dependent transition of quantized spin-wave modes in Ni₈₀Fe₂₀ square nanorings, *J. Appl. Phys.* **116**, 163912 (2014).

- [71] J. Walowski, M. D. Kaufmann, B. Lenk, C. Hamann, J. McCord, and M. Münzenberg, Intrinsic and non-local Gilbert damping in polycrystalline nickel studied by Ti : sapphire laser fs spectroscopy, *J. Phys. D: Appl. Phys.* **41**, 164016 (2008).
- [72] D. M. Lattery, D. Zhang, J. Zhu, P. Crowell, J. Wang, and X. Wang, Optimization of time-resolved magneto-optical Kerr effect signals for magnetization dynamics measurements, [arXiv:1803.01280](https://arxiv.org/abs/1803.01280).
- [73] D. M. Lattery, D. Zhang, J. Zhu, X. Hang, J. Wang, and X. Wang, Low Gilbert damping constant in perpendicularly magnetized W/CoFeB/MgO films with high thermal stability, *Sci. Rep.* **8**, 13395 (2018).
- [74] B. Heinrich and J. A. C. Bland, Spin relaxation in magnetic metallic layers and multilayers, in *Ultrathin Magnetic Structures: Fundamentals of Nanomagnetism* (Springer, New York, 2005).
- [75] J. Wu, N. D. Hughes, J. R. Moore, and R. J. Hicken, Excitation and damping of spin excitations in ferromagnetic thin films, *J. Magn. Magn. Mater.* **241**, 96 (2002).
- [76] P. Nieves, D. Serantes, U. Atxitia, and O. Chubykalo-Fesenko, Quantum Landau-Lifshitz-Bloch equation and its comparison with the classical case, *Phys. Rev. B* **90**, 104428 (2014).
- [77] Y. Liu, L. R. Shelford, V. V. Kruglyak, R. J. Hicken, Y. Sakuraba, M. Oogane, and Y. Ando, Optically induced magnetization dynamics and variation of damping parameter in epitaxial Co₂MnSi Heusler alloy films, *Phys. Rev. B* **81**, 094402 (2010).
- [78] J. Walowski, G. Muller, M. Djordjevic, M. Münzenberg, M. Klaui, C. A. F. Vaz, and J. A. C. Bland, Energy equilibration processes of electrons, magnons, and phonons at the femtosecond time scale, *Phys. Rev. Lett.* **101**, 237401 (2008).
- [79] Y. Ren, Y. L. Zuo, M. S. Si, Z. Z. Zhang, Q. Y. Jin, and S. M. Zhou, Correlation between ultrafast demagnetization process and Gilbert damping in amorphous TbFeCo Films, *IEEE Trans. Magn.* **49**, 3159 (2013).